RSC Advances

PAPER

View Article Online
View Journal | View Issue

Cite this: *RSC Adv.*, 2016, **6**, 52646

$Na_{0.5}Ce_{0.5}MoO_4$ as a new light absorption material to efficiently degrade RhB under visible light irradiation†

Liming Yang, Fei Teng,* Juan Xu, Yang Yang, Yandong Kan and Wenhao Gu

Received 21st March 2016
Accepted 22nd May 2016

DOI: 10.1039/c6ra07362j

www.rsc.org/advances

It still remains a big challenge to develop an efficient visible light responsive photocatalyst for the full utilization of solar energy. In this work, $Na_{0.5}Ce_{0.5}MoO_4$ has been developed as a new, high visible light absorption medium and a high electron-conducting material. It has greatly improved the visible light absorbance and the charge separation and transfer rates of the $Na_{0.5}Ce_{0.5}MoO_4/MoO_3$ heterojunction. Amazingly, the activity of $Na_{0.5}Ce_{0.5}MoO_4$ (10%)/MoO_3 is 6.4 times higher than that of MoO_3 for the photodegradation of RhB under visible light irradiation ($\lambda \geq 420$ nm). We expect that $Na_{0.5}Ce_{0.5}MoO_4$ could be applied to prepare other excellent visible light heterojunction photocatalysts to fully utilize solar energy.

1. Introduction

Today, dyestuff wastewater pollution is a great threat to human health and the ecosystem and has attracted public concern widely. In recent years, semiconductor photocatalysis has been put forward as an effective way to solve the pollution problem.[1–4] TiO_2, as an important photocatalyst for the decomposition of hazardous organic pollutants, has been studied extensively.[5,6] However, TiO_2 can only absorb UV light, whose proportion is only 4% of sunlight, which limits its practical applications.[7–9] Therefore, it is desirable to develop visible light responsive semiconductor photocatalysts.

In recent years, the rare earth compounds have received extensive attention because of their technological applications in high-performance luminescent devices, magnet, catalysts and the other functional materials, due to the novel optoelectronic and chemical properties originating from their 4f shell.[10] Among various rare earth compounds, $ARE(MoO_4)_2$ (A = Na, K, RE = trivalent rare earth ion) exhibit an excellent thermal and hydrolytic stability, and can be widely used in quantum electronics and efficient phosphors.[11,12] Up to now, the application studies of $ARE(MoO_4)_2$ are still limited in the luminescence field. Xu *et al.* synthesized $NaCe(MoO_4)_2$ flowers, which was used as absorbents for removal of RhB.[13] Molybdenum trioxide (MoO_3), as an n-type semiconductor, is an important electrochromic and photochromic sensitive material as gas sensors and optical devices.[14–16] Recently, the photocatalytic activity of MoO_3 has been reported for the organic pollutants degradation.[17–19] As far as we know, α-MoO_3 has the band gap of 2.92 eV, which can mainly absorb UV light, but only absorb less visible light.[20] Moreover, the high recombination rate of photogenerated charges of MoO_3 has greatly hampered its practical applications.[21,22] To date, many efforts have been made to improve its photocatalytic activity by coupling MoO_3 with the other semiconductors, such as TiO_2–MoO_3, Ag–MoO_3, rGO/C–MoO_3 and g-C_3N_4–MoO_3.[23–26] However, these MoO_3-based composites can still not utilize the visible light effectively, or the load of noble metal would increase the expense. Thus, it still remains a big challenge to further improve the photocatalytic properties of MoO_3 under visible light.

In this work, $Na_{0.5}Ce_{0.5}MoO_4$ as a new material is introduced to the field of photocatalysis for the first time. A new visible light-responsive $Na_{0.5}Ce_{0.5}MoO_4/MoO_3$ is synthesized successfully *via* one-pot hydrothermal process and calcination treatment. It not only can efficiently absorb visible light, but also has a high electrical conductivity. For $Na_{0.5}Ce_{0.5}MoO_4/MoO_3$ composites, they all clearly exhibit higher visible light absorption than MoO_3 and can effectively excite more photo-generated carriers. In addition, MoO_3 and $Na_{0.5}Ce_{0.5}MoO_4$ have the matched energy bands; thus, a stable heterojunction is easy to form between them. And $Na_{0.5}Ce_{0.5}MoO_4$ presents a high conductivity which favors for the transportation and separation of photogenerated carries. As a result, $Na_{0.5}Ce_{0.5}MoO_4/MoO_3$ composites improve the photocatalytic activities under visible light. Finally, a possible mechanism of the enhanced visible light photocatalytic activity is put forward. Until now, few

Jiangsu Engineering and Technology Research Center of Environmental Cleaning Materials (ECM), Jiangsu Key Laboratory of Atmospheric Environment Monitoring and Pollution Control (AEMPC), Jiangsu Joint Laboratory of Atmospheric Pollution Control (APC), Collaborative Innovation Center of Atmospheric Environment and Equipment Technology (AEET), School of Environmental Science and Engineering, Nanjing University of Information Science & Technology, 219 Ningliu Road, Nanjing 210044, China. E-mail: tfwd@163.com; Fax: +86-25-9882-1090; Tel: +86-25-9882-1090

† Electronic supplementary information (ESI) available. See DOI: 10.1039/c6ra07362j

studies have been reported on $Na_{0.5}Ce_{0.5}MoO_4/MoO_3$ composites. We could expect that $Na_{0.5}Ce_{0.5}MoO_4$, as a new visible light absorbance and charge transfer medium, could be applied to prepare the other excellent visible light-responsive composite photocatalysts.

2. Experimental section

2.1 Catalyst preparation

All reagents were of analytical grade, purchased from Beijing Chemical Reagents Industrial Company of China, and were used without further purification in all our experiments. In a typical procedure, 2 mmol of $Na_2MoO_4 \cdot 2H_2O$ was added into 30 mL of distilled water and then 10 mmol of thiourea was added into the above solution. After the $Na_2MoO_4 \cdot 2H_2O$ and thiourea was fully dissolved, an appropriate amount of $Ce(NO_3)_3 \cdot 6H_2O$ was added into the above solution and stirred for 60 min by a magnetic stirrer at room temperature. Subsequently, the mixture was transferred into a Teflon-lined stainless steel autoclave and maintained at 180 °C for 48 h. After the autoclave was allowed to cool to room temperature, the as-obtained product was filtered, washed with absolute ethanol and distilled water several times, and subsequently dried at 60 °C for 6 h. After that, the as-obtained product was calcined in air at 400 °C for 2 h. A series of $Na_{0.5}Ce_{0.5}MoO_4/MoO_3$ with the different mass ratios were prepared by adjusting the concentrations of Ce or MoO_4^{2-} ions. The as-prepared samples with different mass ratios were denoted as $x$$Na_{0.5}Ce_{0.5}MoO_4/MoO_3$, where x refers to the mass ratios of $Na_{0.5}Ce_{0.5}MoO_4$ to MoO_3 (x = 0%, 10%, 20%, 40%, 60%, 80%, 100%).

For comparison, phase-pure MoO_3 was also prepared under the same conditions as above but without adding $Ce(NO_3)_3 \cdot 6H_2O$. The pure-phase $Na_{0.5}Ce_{0.5}MoO_4$ sample was prepared with 2 mmol Na_2MoO_4 and 0.5 mmol $Ce(NO_3)_3 \cdot 6H_2O$ under the hydrothermal condition of 180 °C for 24 h.

To evaluate the role of heterojunction on the photocatalytic activity of the $Na_{0.5}Ce_{0.5}MoO_4/MoO_3$, a mechanically mixed $Na_{0.5}Ce_{0.5}MoO_4$ and MoO_3 (denoted as $Na_{0.5}Ce_{0.5}MoO_4 + MoO_3$) was prepared and evaluated.

2.2 Characterization

The crystal structures of the samples were determined by X-ray powder polycrystalline diffractometer (Rigaku D/max-2550VB), using graphite monochromatized Cu K_α radiation (λ = 0.154 nm), operating at 40 kV and 50 mA. The XRD patterns were obtained in the range of 20–80° (2θ) at a scanning rate of 5° min^{-1}. The samples were characterized on a scanning electron microscope (SEM, Hitachi SU-1510) with an acceleration voltage of 15 keV. The samples were coated with 5 nm-thick gold layer before observations. The fine surface structures of the samples were determined by high-resolution transmission electron microscopy (HRTEM, JEOL JEM-2100F) equipped with an electron diffraction (ED) attachment with an acceleration voltage of 200 kV. UV-vis diffused reflectance spectra of the samples were obtained using a UV-vis spectrophotometer (UV-2550, Shimadzu, Japan). $BaSO_4$ was used as a reflectance standard in a UV-vis diffuse reflectance experiment. Photoluminescence (PL) spectra were measured on a fluorescence spectrophotometer (Japan, Shimadzu RF-5301PC) with the 265 nm excitation line of a Xe lamp as the excitation source. Nitrogen sorption isotherms were performed at 77 K and $<10^{-4}$ bar on a Micromeritics ASAP2010 gas adsorption analyzer. Each sample was degassed at 150 °C for 5 h before measurements. Surface area was calculated by the Brunauer–Emmett–Teller (BET) method.

2.3 Transient photocurrents and electrochemical impedance spectroscopy (EIS)

An electrochemical system (CHI-660B, China) was employed to measure the photocurrents and electrochemical impedance spectroscopy (EIS). Electrochemical impedance spectroscopy (EIS) was performed from 0.1 Hz to 100 kHz at an open circuit potential of 0.3 V and an alternating current (AC) voltage amplitude of 5 mV. The data were analyzed by ZSimpWin software. Photocurrent measurements were carried out in a conventional three-electrode system, in which indium-tin oxide (ITO) glass was used as the current collector to fabricate photo electrode, and 0.5 M Na_2SO_4 was used as the electrolyte solution. MoO_3/ITO, $x$$Na_{0.5}Ce_{0.5}MoO_4/MoO_3$/ITO and $Na_{0.5}Ce_{0.5}MoO_4$/ITO photo electrode were prepared by a coating method.

2.4 Photocatalytic degradation reaction

The photocatalytic activities of the samples were evaluated by the decomposition of Rhodamine B (RhB) under visible light ($\lambda \geq 420$ nm), using a 500 W Xe arc lamp (CEL-HXF 300) equipped with a visible cutoff filter as a light source. The reaction system was placed in a sealed black box with the top opened, and was maintained a distance of 15 cm from the light source. In a typical photocatalytic experiment, the photocatalyst powder (100 mg) was suspended in 200 mL of the RhB aqueous solution, with an initial concentration of 10 mg L^{-1}. Before irradiation, the suspension (200 mL) was stirred for 30 min in the dark to ensure the establishment of an adsorption–desorption equilibrium between the photocatalyst and RhB solution, and then irradiated with a 500 W Xe arc lamp equipped with visible light ($\lambda \geq 420$ nm). During photoreaction, 3 mL of suspension was collected at intervals of irradiation by pipette, and subsequently centrifuged to remove the catalysts. UV-vis spectra were recorded on a Spectrumlab 722 sp spectrophotometer to determine the concentration of RhB.

In order to investigate reactive species, the trapping experiment was performed, in which holes (h^+) and hydroxyl radical ($^{\bullet}OH$) were trapped by adding 1 mM ammonium oxalate ($(NH_4)_2C_2O_4$) and 10 mL dimethyl sulfoxide (DMSO) into the RhB solution, respectively.

3. Results and discussion

3.1 Physicochemistry characterization of photocatalyst

Fig. 1 shows XRD patterns of the as-prepared samples. The strong diffraction peaks indicate the high crystallinity of the as-prepared products. The diffraction peaks at 2θ = 12.8°, 23.4°,

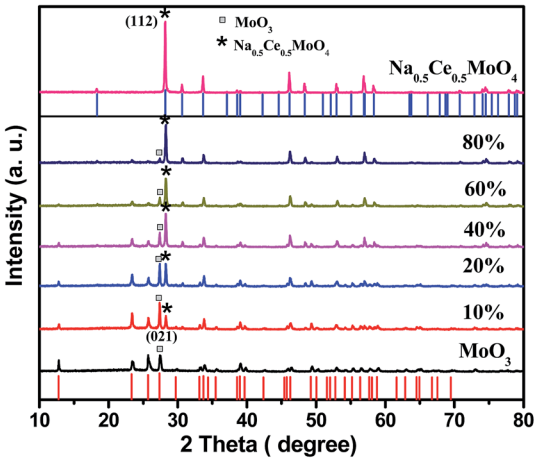

Fig. 1 X-ray diffraction (XRD) patterns of MoO_3, $Na_{0.5}Ce_{0.5}MoO_4$ and $xNa_{0.5}Ce_{0.5}MoO_4/MoO_3$ samples, where x refers to the mass ratio of $Na_{0.5}Ce_{0.5}MoO_4$ to MoO_3.

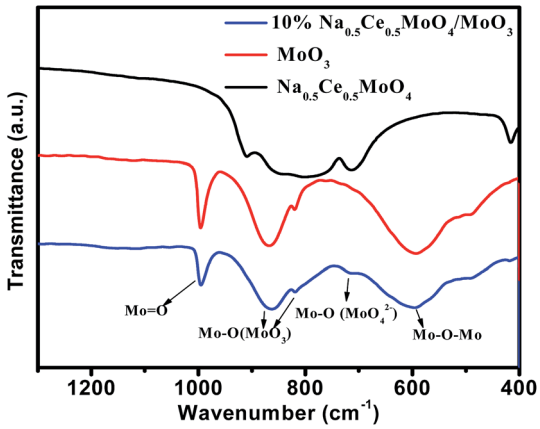

Fig. 2 Fourier transform infrared (FT-IR) spectra of MoO_3, $Na_{0.5}Ce_{0.5}MoO_4$ and 10% $Na_{0.5}Ce_{0.5}MoO_4/MoO_3$.

25.8°, 27.4° and 33.8° correspond to (020), (110), (040), (021) and (111) crystal planes of orthorhombic MoO_3 (JCPDS card no. 05-0508), respectively. The results confirm the formation of phase-pure MoO_3. The diffraction peaks at $2\theta = 18.3°$, 28.2°, 30.6°, 33.6° and 46.2° can be perfectly indexed to the (101), (112), (004), (200) and (204) crystal planes of tetragonal $Na_{0.5}Ce_{0.5}MoO_4$ with a space group of $I4_1/a$ (JCPDS card no. 79-2242),[13] respectively. This results confirm the formation of phase-pure $Na_{0.5}Ce_{0.5}MoO_4$. For $Na_{0.5}Ce_{0.5}MoO_4/MoO_3$ composites, the XRD patterns clearly indicate the co-existence of MoO_3 and $Na_{0.5}Ce_{0.5}MoO_4$ in the as-prepared nanocomposites, and no impurity phases are observed. With increasing content of $Na_{0.5}Ce_{0.5}MoO_4$, (112) peak intensity of $Na_{0.5}Ce_{0.5}MoO_4$ at $2\theta = 28.2°$ increases quickly, meanwhile (021) peak intensity of MoO_3 at $2\theta = 27.4°$ decreases gradually. Table 1 shows that the peak intensity ratios of MoO_3 to $Na_{0.5}Ce_{0.5}MoO_4$ decrease clearly.

Fig. 2 shows FT-IR spectra of $Na_{0.5}Ce_{0.5}MoO_4$, MoO_3 and 10% $Na_{0.5}Ce_{0.5}MoO_4/MoO_3$. For orthorhombic α-MoO_3, the sharp band at about 996 cm^{-1} is assigned as the stretching vibration of Mo=O; the band at about 867 cm^{-1} and 595 cm^{-1} are associated with the vibration of bridging Mo–O–Mo bonds and Mo–O bands, respectively.[27–29] For pure $Na_{0.5}Ce_{0.5}MoO_4$, one abroad peak in 950–700 cm^{-1} is resultant from the Mo–O stretching vibration in MoO_4^{2-}.[30] In the case of 10% $Na_{0.5}Ce_{0.5}MoO_4/MoO_3$ sample, the characteristic bands of both $Na_{0.5}Ce_{0.5}MoO_4$ and MoO_3 can be observed clearly. XRD and FT-IR results confirm that the formation of $Na_{0.5}Ce_{0.5}MoO_4/MoO_3$ composite.

The morphology of the samples was characterized by SEM. Fig. 3 shows the SEM images of the samples. The as-prepared MoO_3 sample is composed of nanosheets, which are about 250–300 nm thick (Fig. 3a). 10% $Na_{0.5}Ce_{0.5}MoO_4/MoO_3$ sample is composed of many sheets of 600–1200 nm thick and some of small particles (Fig. 3b). Compare with pure MoO_3, the sheet thickness increases clearly. We assume that MoO_3 sheets may be coated by $Na_{0.5}Ce_{0.5}MoO_4$ particles. With further increasing the amount of $Na_{0.5}Ce_{0.5}MoO_4$, most of MoO_3 sheets have broken into small irregular pieces and more nanoparticles have appeared (Fig. 3b and c). Obviously, the coexistence of $Na_{0.5}Ce_{0.5}MoO_4$ and MoO_3 did significantly affect their morphologies. Moreover, as the mass ratio of $Na_{0.5}Ce_{0.5}MoO_4$ is varied from 20% to 80%, the number of nanoparticles coated on MoO_3 increases dramatically (Fig. 3d–f). These indicate that $Na_{0.5}Ce_{0.5}MoO_4$ nanoparticles have formed. The morphology of $Na_{0.5}Ce_{0.5}MoO_4$ is presented in the ESI, Fig. S1.† Furthermore, the Brunauer–Emmett–Teller (BET) areas of the samples are presented in Table 2. Among them, 10% $Na_{0.5}Ce_{0.5}MoO_4/MoO_3$ has a larger surface area (8.5 $m^2\ g^{-1}$) than $Na_{0.5}Ce_{0.5}MoO_4$ (6.1 $m^2\ g^{-1}$), while the others are smaller than pure $Na_{0.5}Ce_{0.5}MoO_4$. However, the surface areas of $Na_{0.5}Ce_{0.5}MoO_4/MoO_3$ composites are all higher than that (2.4 $m^2\ g^{-1}$) of MoO_3. This can be attributed to the generation of nanoparticles.

Table 1 Peak intensity ratios of $xNa_{0.5}Ce_{0.5}MoO_4/MoO_3$ samples with different weight ratios[a]

Sample	(021) peak intensity of MoO_3 at $2\theta = 27.36°$	(112) peak intensity of $Na_{0.5}Ce_{0.5}MoO_4$ at $2\theta = 28.26°$	Peak intensity ratio of (021) MoO_3/(112) $Na_{0.5}Ce_{0.5}MoO_4$
10%	560	390	1.436
20%	495	545	0.908
40%	236	812	0.291
60%	187	937	0.200
80%	60	782	0.077

[a] x: the mass ratio of $Na_{0.5}Ce_{0.5}MoO_4$ to MoO_3.

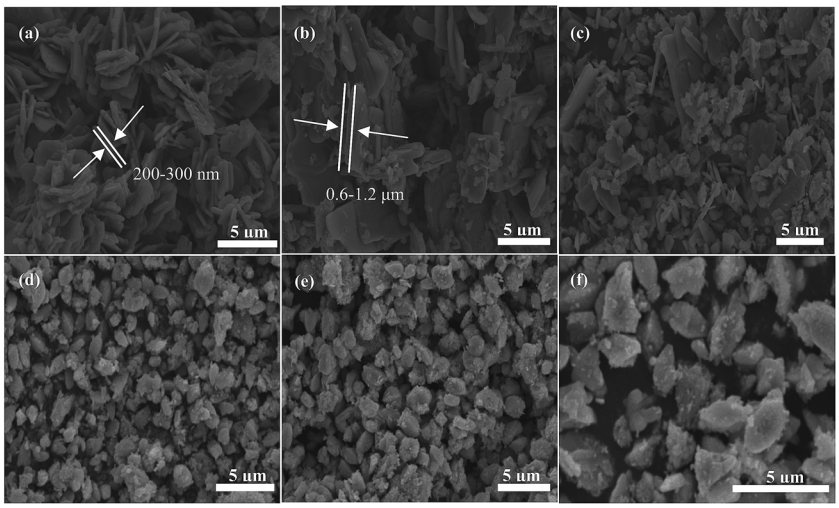

Fig. 3 Scanning electron microscopy (SEM) images of MoO_3 and $xNa_{0.5}Ce_{0.5}MoO_4/MoO_3$ samples: (a) MoO_3; (b) $x = 10\%$; (c) $x = 20\%$; (d) $x = 40\%$; (e) $x = 60\%$; (f) $x = 80\%$.

Table 2 Specific surface areas, band gap (E_g) values and apparent first-order rate constant of the samples for the degradation of RhB under visible light ($\lambda \geq 420$ nm)

Sample	BET area[a] ($m^2\ g^{-1}$)	Band gap (E_g, eV)	k_{app}[b] (min^{-1})
MoO_3	2.442	2.92	0.003
$Na_{0.5}Ce_{0.5}MoO_4$	6.033	2.58	9.93×10^{-4}
10%	8.513	2.74	0.0221
20%	4.883	2.67	0.0206
40%	2.983	2.64	0.0177
60%	3.155	2.54	0.0129
80%	4.134	2.52	0.0044

[a] Calculated by the Brunauer–Emmett–Teller (BET) method. [b] k_{app} is the rate constants of pseudo first order (min^{-1}).

The fine surface structures of the 10% and 60% $Na_{0.5}Ce_{0.5}MoO_4/MoO_3$ are further characterized by high-resolution transmission electron microscopy (HRTEM). Fig. 4a and d show the TEM images of 10% and 60% $Na_{0.5}Ce_{0.5}MoO_4/MoO_3$, respectively. It could be clearly observed that numerous nanoparticles have deposited on the surface of MoO_3 sheets, consistent with SEM observation. In addition, Fig. 4b and e show their lattice fringe images. For 10% $Na_{0.5}Ce_{0.5}MoO_4/MoO_3$ (Fig. 4b), the lattice fringe spacings of 0.27 nm and 0.292 nm coincide with (101) plane of MoO_3 and (004) plane of $Na_{0.5}Ce_{0.5}MoO_4$, respectively. For 60% $Na_{0.5}Ce_{0.5}MoO_4/MoO_3$ (Fig. 4e), the lattice fringe spacing of 0.315 nm coincides with (112) crystal plane of $Na_{0.5}Ce_{0.5}MoO_4$. Meanwhile, the lattice fringe spacing of 0.326 nm coincides with (021) crystal plane of MoO_3. Besides, Fig. 4c and f show the selected area electron diffraction (SAED) patterns of both samples. In Fig. 4c, two sets of diffraction spots are clearly observed. The distances from two diffraction spots to the center are determined to be 1.96 nm and 2.92 nm, corresponding to the inter-plane spacings of (204) and (004) of $Na_{0.5}Ce_{0.5}MoO_4$, respectively; and the distances from the diffraction spots to the center are 2.7 nm and 3.8 nm, corresponding to the inter-plane spacings of (101) and (110) of MoO_3, respectively. Likewise, in Fig. 4f, the clear diffraction spots can be ascribed to the (112) and (004) Bragg reflections of $Na_{0.5}Ce_{0.5}MoO_4$, and the (040) and (021) Bragg reflections of MoO_3, respectively. The diffraction peaks of these planes also appear at 28.3° and 30.6° ($Na_{0.5}Ce_{0.5}MoO_4$) and 25.8° and 27.4° for MoO_3 in the XRD patterns. Hence, these observations firmly demonstrate that the formation of intimate heterojunction between $Na_{0.5}Ce_{0.5}MoO_4$ and MoO_3. This intimate heterojunction structure would favor for the charge separation, thus effectively improving the photocatalytic activity.

3.2 Excellent visible light absorbing ability of $Na_{0.5}Ce_{0.5}MoO_4$

Fig. 5a shows the ultraviolet-visible light diffuse reflectance spectra (UV-DRS) of the samples. The pure MoO_3 shows the absorption edge at about 425 nm, which corresponds to a band gap energy of 2.92 eV; while the absorption edge of pure $Na_{0.5}Ce_{0.5}MoO_4$ is about 504 nm. Obviously, the UV-DRS spectra of $Na_{0.5}Ce_{0.5}MoO_4/MoO_3$ composites clearly show the spectrum combination of both $Na_{0.5}Ce_{0.5}MoO_4$ and MoO_3, and the absorption edge of the $Na_{0.5}Ce_{0.5}MoO_4/MoO_3$ composites show a shift toward visible region gradually. Significantly, the presence of $Na_{0.5}Ce_{0.5}MoO_4$ improves the visible light absorption ability of $Na_{0.5}Ce_{0.5}MoO_4/MoO_3$ composites and greatly extends the absorption range of visible light, which is favorable for $Na_{0.5}Ce_{0.5}MoO_4/MoO_3$ to generate more electron–hole pairs under visible light irradiation. Thus it may be one of the reasons that affect the photocatalytic performance. Furthermore, Tauc plots of MoO_3, $Na_{0.5}Ce_{0.5}MoO_4$ and 10% $Na_{0.5}Ce_{0.5}MoO_4/MoO_3$ is shown in Fig. 5b. Based on the UV-DRS results, the E_g is calculated by eqn (1) as follows:[31]

$$\alpha h\nu = A(h\nu - E_g)^{n/2} \quad (1)$$

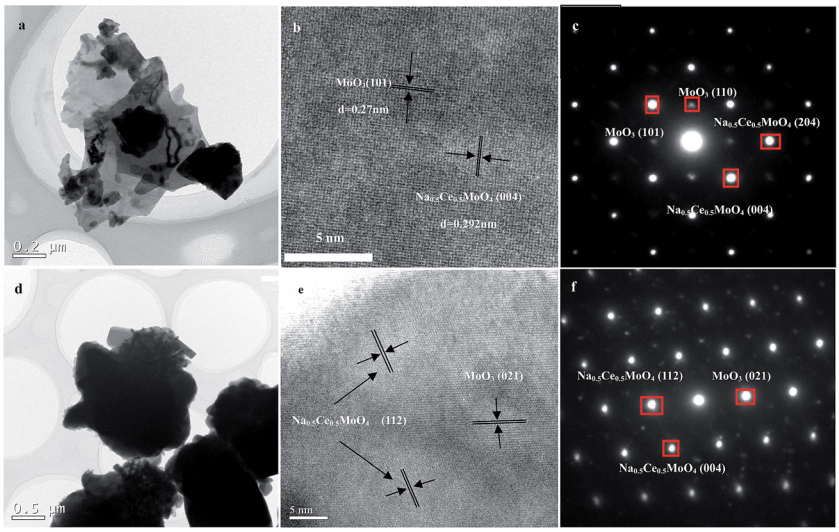

Fig. 4 High-resolution transmission electron microscopy (HRTEM) images and selected area electron diffraction (SAED) patterns of xNa$_{0.5}$Ce$_{0.5}$MoO$_4$/MoO$_3$ samples: (a–c) x = 10%; (d–f) x = 60%.

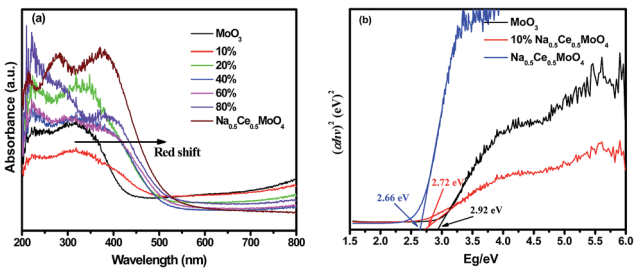

Fig. 5 (a) UV-visible diffuse reflectance spectra (UV-DRS) of the samples; (b) Tauc plots of MoO$_3$, Na$_{0.5}$Ce$_{0.5}$MoO$_4$ and 10% Na$_{0.5}$Ce$_{0.5}$MoO$_4$/MoO$_3$.

where α, h, ν, E_g and A are absorption coefficient, Plank constant, light frequency, band gap energy and a constant, respectively. Among them, n is determined by the type of optical transition of a semiconductor ($n = 1$ for direct transition and $n = 4$ for indirect transition). For MoO$_3$, the value of n is taken as 1, and the E_g value of MoO$_3$ is estimated to be 2.92 eV according to a plot of $(\alpha h\nu)^2$ *versus* energy ($h\nu$).[32] Accordingly, E_g values of Na$_{0.5}$Ce$_{0.5}$MoO$_4$ and 10% Na$_{0.5}$Ce$_{0.5}$MoO$_4$/MoO$_3$ are 2.66 eV and 2.72 eV, respectively. Moreover, it found that the band gaps of Na$_{0.5}$Ce$_{0.5}$MoO$_4$/MoO$_3$ heterojunctions range from 2.67 eV to 2.52 eV, which gradually decreases with the increase of Na$_{0.5}$Ce$_{0.5}$MoO$_4$ content from 20% to 80% (Table 2).

Furthermore, the conduction band (CB) and valence band (VB) potentials of MoO$_3$ and Na$_{0.5}$Ce$_{0.5}$MoO$_4$ are calculated by the following equations:[33]

$$E_{VB} = \chi - E^c + 0.5E_g \quad (2)$$

$$E_{CB} = E_{VB} - E_g \quad (3)$$

where E_{VB} is the potential of valence band edge, E_{CB} is the potential of conduction band edge, χ is the electronegativity of semiconductor, which is the geometric mean of the electronegativity of constituent atoms, E^c is the energy of free electrons on the hydrogen scale (about 4.5 eV), E_g is the band gap energy of semiconductor. According to the above equations, the bottom of conduction band (CB) and the top of valance band (VB) of Na$_{0.5}$Ce$_{0.5}$MoO$_4$ are −0.06 eV and 2.60 eV, while those of MoO$_3$ are 0.44 eV and 3.36 eV, respectively, which is similar to the reported literature.[34] Therefore, MoO$_3$ and Na$_{0.5}$Ce$_{0.5}$MoO$_4$ have matched energy bands; and a stable heterojunction is easy to form between them.

3.3 High electrical conductivity of Na$_{0.5}$Ce$_{0.5}$MoO$_4$

The electrochemical impedance spectroscopy (EIS) is measured to investigate the effect of Na$_{0.5}$Ce$_{0.5}$MoO$_4$ on the electron transfer properties. As we all know, the transportation and separation efficiencies of photo-generated charges have a significant influence on photocatalytic activity.[35,36] The arc radius in the EIS spectra reflects the solid-state surface charge transfer resistance, and a smaller semicircle radius in the EIS Nyquist plot means a smaller electric resistance, which favors for electron transportation.[37] As a result, the fast electron transfer rate favors the efficient separation of photo-generated electrons and holes.[38,39] As shown in Fig. 6, the Nyquist radius of Na$_{0.5}$Ce$_{0.5}$MoO$_4$ is obviously smaller than that of MoO$_3$, indicating that Na$_{0.5}$Ce$_{0.5}$MoO$_4$ has a greatly higher conductivity than MoO$_3$, which favors for the transportation and separation of photogenerated carriers. For xNa$_{0.5}$Ce$_{0.5}$MoO$_4$/MoO$_3$ samples, they all have a smaller Nyquist radius than MoO$_3$, and 10% Na$_{0.5}$Ce$_{0.5}$MoO$_4$/MoO$_3$ photocatalyst has the smallest surface resistance among them. These results indicate that compared with pure MoO$_3$, the presence of Na$_{0.5}$Ce$_{0.5}$MoO$_4$ can reduce the electric resistance and promote the transfer and separation of photogenerated carriers, thus improving the photocatalytic activity of Na$_{0.5}$Ce$_{0.5}$MoO$_4$/MoO$_3$ samples.

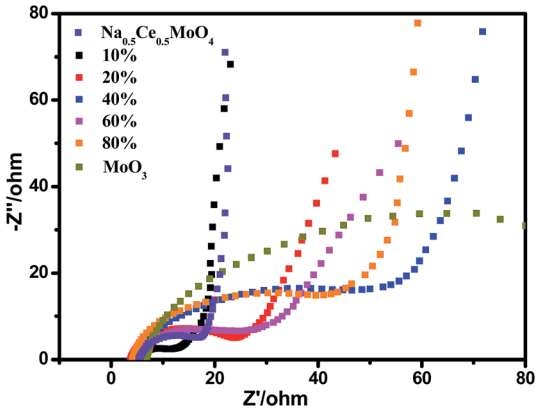

Fig. 6 Nyquist plots of MoO_3, $Na_{0.5}Ce_{0.5}MoO_4$ and $xNa_{0.5}Ce_{0.5}MoO_4/MoO_3$ samples in the frequency range of 0.1–10^6 Hz.

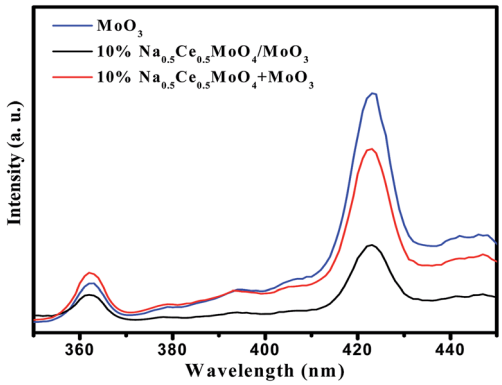

Fig. 8 Photoluminescence emission spectra (PL) of MoO_3, 10% $Na_{0.5}Ce_{0.5}MoO_4/MoO_3$, and mechanical mixed 10% $Na_{0.5}Ce_{0.5}MoO_4$ + MoO_3 at excitation wavelength of 265 nm.

Transient photocurrent response directly correlate with the transportation and separation efficiencies of photo-generated carriers.[40] In order to investigate the photocurrent property, the *I*–*t* curves of MoO_3, $Na_{0.5}Ce_{0.5}MoO_4$, 10% $Na_{0.5}Ce_{0.5}MoO_4/MoO_3$, and mechanical mixed 10% $Na_{0.5}Ce_{0.5}MoO_4$ + MoO_3 are recorded under visible light irradiation ($\lambda \geq 420$ nm) (Fig. 7). The photocurrent values clearly return to a constant value while the light is turned on. Compared with $Na_{0.5}Ce_{0.5}MoO_4$, MoO_3 and 10% $Na_{0.5}Ce_{0.5}MoO_4$ + MoO_3, the 10% $Na_{0.5}Ce_{0.5}MoO_4/MoO_3$ exhibits a higher transient photocurrent density (about 4 μA cm^{-2}), which is about 5 times as high as that (about 0.8 μA cm^{-2}) of MoO_3. Compared with 10% $Na_{0.5}Ce_{0.5}MoO_4$ + MoO_3, the enhanced photocurrent of 10% $Na_{0.5}Ce_{0.5}MoO_4/MoO_3$ indicates that there is a strong interaction between $Na_{0.5}Ce_{0.5}MoO_4$ and MoO_3, which favors for efficient carrier separation at the interface. On the other hand, $Na_{0.5}Ce_{0.5}MoO_4$ has a high electrical conductivity, as a result, which can greatly promote the charges transfer and increase the separation rate of charges.

The photoluminescence emission spectrum (PL) of semiconductor could reflect the recombination probability of photogenerated electrons and holes.[41,42] Fig. 8 shows the PL spectra of pure MoO_3, 10% $Na_{0.5}Ce_{0.5}MoO_4/MoO_3$ and 10% $Na_{0.5}Ce_{0.5}MoO_4$ + MoO_3 at excitation wavelength of 265 nm. The PL spectra of the other samples are shown in Fig. S2 (ESI†). It is obvious that two main emission peaks of MoO_3 at about 362 nm and 425 nm are evidently decreased in intensity in the presence of $Na_{0.5}Ce_{0.5}MoO_4$. Compared with 10% $Na_{0.5}Ce_{0.5}MoO_4$ + MoO_3, it could further confirm the existence of heterojunction between $Na_{0.5}Ce_{0.5}MoO_4$ and MoO_3. Moreover, the presence of $Na_{0.5}Ce_{0.5}MoO_4$ can reduce the electric resistance and promote the transfer of charges, thus improving the separation efficiency of photogenerated carriers significantly.

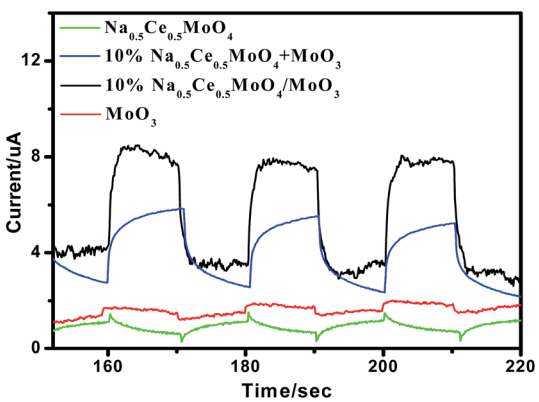

Fig. 7 Transient photocurrent density of MoO_3, $Na_{0.5}Ce_{0.5}MoO_4$, 10% $Na_{0.5}Ce_{0.5}MoO_4/MoO_3$ and mechanical mixed 10% $Na_{0.5}Ce_{0.5}MoO_4$ + MoO_3 under visible light irradiation ($\lambda \geq 420$ nm).

3.4 Photocatalytic activity

The photocatalytic activities of the samples were evaluated by the photodegradation of RhB under visible light irradiation ($\lambda \geq 420$ nm). Prior to light irradiation, the suspension was magnetically stirred in the dark for about 30 min to reach the absorption–desorption equilibrium between RhB and the photocatalyst. It can be seen from Fig. 9a that all the $Na_{0.5}Ce_{0.5}MoO_4/MoO_3$ samples exhibit higher photocatalytic activities than MoO_3 and $Na_{0.5}Ce_{0.5}MoO_4$. After 90 min of visible light irradiation ($\lambda \geq 420$ nm), the RhB degradation over phase-pure MoO_3 and $Na_{0.5}Ce_{0.5}MoO_4$ is only 24% and 10%, respectively. Interestingly, after coupling $Na_{0.5}Ce_{0.5}MoO_4$ with MoO_3, the RhB degradation is clearly increased. For example, 10%, 20% and 40% $Na_{0.5}Ce_{0.5}MoO_4/MoO_3$ could respectively degrade 94%, 85% and 84.8% of RhB in 90 min of visible light irradiation ($\lambda \geq 420$ nm). The results show that the presence of $Na_{0.5}Ce_{0.5}MoO_4$ can effectively enhance the photocatalytic activity of $Na_{0.5}Ce_{0.5}MoO_4/MoO_3$ composites. However, the degradation efficiency gradually decreases with increasing amount of $Na_{0.5}Ce_{0.5}MoO_4$. When the $Na_{0.5}Ce_{0.5}MoO_4$ mass ratio is increased to 80%, only 39% of RhB could be degraded in 90 min. Under the same experimental condition, we also have added the blank run, and the self-degradation of RhB is about 4% after 90 min under visible light irradiation ($\lambda \geq 420$ nm). As we mentioned above, pure $Na_{0.5}Ce_{0.5}MoO_4$ has a poor photocatalytic activity under visible light irradiation, but $Na_{0.5}Ce_{0.5}MoO_4$ could efficiently absorb visible light, which is expected to act as an efficient light harvester to generate photo-generated

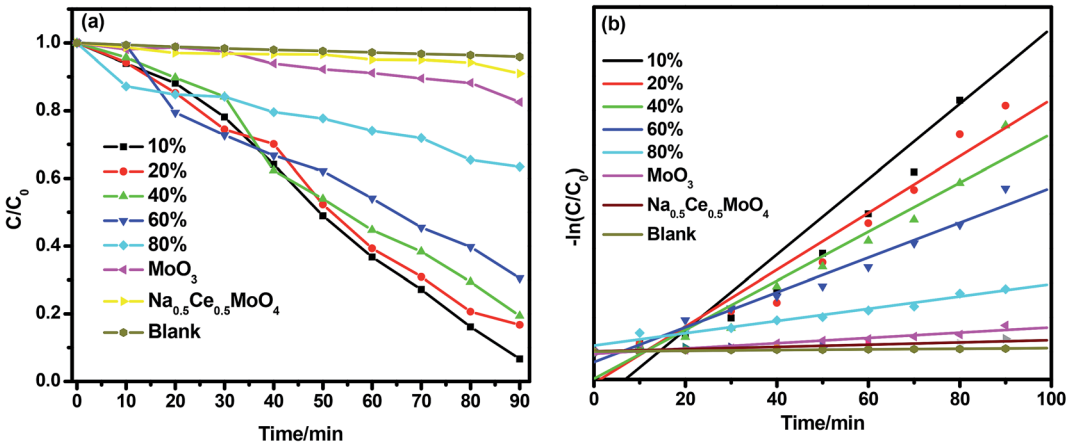

Fig. 9 (a) Photodegradation and (b) kinetic curves of RhB over MoO_3, $Na_{0.5}Ce_{0.5}MoO_4$ and $xNa_{0.5}Ce_{0.5}MoO_4/MoO_3$ samples under visible light irradiation ($\lambda \geq 420$ nm).

carriers. So we assume that an excess amount of $Na_{0.5}Ce_{0.5}MoO_4$ in $Na_{0.5}Ce_{0.5}MoO_4/MoO_3$ composites would absorb more light and reduce the efficient absorption of MoO_3 for generating electrons and holes, which may lead to a reduced photocatalytic activity.[43]

Further, the photocatalytic degradation process of organic contaminant can be simplified as a pseudo-first-order kinetic reaction as follow:[44,45]

$$\ln(C_0/C) = k_{\text{app}}t \tag{4}$$

where C_0 is the initial concentration (mg L^{-1}) of RhB while light-on, C is the concentration of RhB at t-min irradiation (mg L^{-1}), and k_{app} is the apparent pseudo-first-order rate constant (min^{-1}). Fig. 9b gives the linear fitted kinetic curves for the degradation of RhB over photocatalysts under visible light irradiation ($\lambda \geq 420$ nm). The determined k_{app} values for degradation of RhB are summarized in Table 2. The k_{app} value over 10% $Na_{0.5}Ce_{0.5}MoO_4/MoO_3$ is the largest among all samples; it is approximately 7- and 22-times higher than those of pure MoO_3 and $Na_{0.5}Ce_{0.5}MoO_4$, respectively. Fig. 10a shows the UV-vis absorption spectra of RhB dye at different irradiation times over 10% $Na_{0.5}Ce_{0.5}MoO_4/MoO_3$. The characteristic absorption peak of RhB locates at 554 nm.[46] It is obvious that the absorption peak has not shifted with reaction time, indicating that RhB may have been effectively degraded.[47] Moreover, we also have conducted the MB photodegradation experiments with MoO_3, $Na_{0.5}Ce_{0.5}MoO_4$ and 10% $Na_{0.5}Ce_{0.5}MoO_4/MoO_3$, and provided the results in Fig. S3 (ESI†). It can be seen from Fig. S3† that 10% $Na_{0.5}Ce_{0.5}MoO_4/MoO_3$ exhibits a higher photocatalytic activity than MoO_3 and $Na_{0.5}Ce_{0.5}MoO_4$ under visible light irradiation ($\lambda \geq 420$ nm). The result is in consistent with that of RhB photodegradation.

To investigate the stability of $Na_{0.5}Ce_{0.5}MoO_4/MoO_3$ under visible light irradiation ($\lambda \geq 420$ nm), the degradation reaction of RhB dye over the 10% $Na_{0.5}Ce_{0.5}MoO_4/MoO_3$ was cycled for three times. As shown in Fig. S4a (ESI†), the degradation efficiency of 10% $Na_{0.5}Ce_{0.5}MoO_4/MoO_3$ was only reduced by 5% after 3 cycles. Furthermore, we also investigated the XRD pattern of the sample after three cycles (Fig. S4b†). The results indicate that the $Na_{0.5}Ce_{0.5}MoO_4/MoO_3$ photocatalyst has a good stability in photocatalytic reaction.

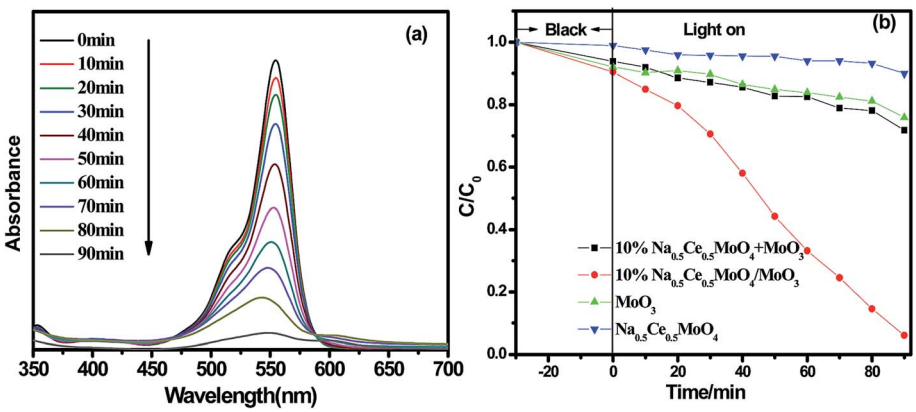

Fig. 10 (a) UV-vis absorption spectra of RhB solution over 10% $Na_{0.5}Ce_{0.5}MoO_4/MoO_3$ sample at different reaction times; (b) photocatalytic activities of MoO_3, $Na_{0.5}Ce_{0.5}MoO_4$, 10% $Na_{0.5}Ce_{0.5}MoO_4/MoO_3$ and mechanical mixed 10% $Na_{0.5}Ce_{0.5}MoO_4$ + MoO_3 on the degradation of RhB under visible-light irradiation ($\lambda \geq 420$ nm).

Furthermore, in order to prove that the visible light photocatalytic activity of $Na_{0.5}Ce_{0.5}MoO_4/MoO_3$ comes from the excitation of the photocatalyst rather than the photosensitization, the degradation of *o*-nitrophenol was also investigated over 10% $Na_{0.5}Ce_{0.5}MoO_4/MoO_3$, MoO_3 and $Na_{0.5}Ce_{0.5}MoO_4$ under visible light irradiation ($\lambda \geq 420$ nm) (Fig. S5, ESI†). It is clear that the 10% $Na_{0.5}Ce_{0.5}MoO_4/MoO_3$ shows a higher activity than MoO_3 and $Na_{0.5}Ce_{0.5}MoO_4$ for the photodegradation of *o*-nitrophenol. The result indicates that the effect of dye sensitization can be avoided. Moreover, the blank run of *o*-nitrophenol has also been tested and the *o*-nitrophenol self-degradation is about 9% after 3 h visible light irradiation ($\lambda \geq 420$ nm), which might be attributed to a small amount of volatile under stirring process. Given in the Table 2, we also show the Brunauer–Emmett–Teller (BET) areas of xNa$_{0.5}$Ce$_{0.5}$MoO$_4$/MoO$_3$ samples. Obviously, 10% $Na_{0.5}Ce_{0.5}MoO_4/MoO_3$ has the largest surface area (8.5 $m^2\ g^{-1}$) among all samples, which could be ascribed to the formation of $Na_{0.5}Ce_{0.5}MoO_4$ nanoparticles. In the process of photodegradation, the larger surface area will be favorable to increase the contact area with organic pollutant, the more active sites will be provided to degrade organic pollutant. Thus it may be one of the reasons that affect the photocatalytic performance.

In addition, to further evaluate the role of heterojunction on the photocatalytic activity of the $Na_{0.5}Ce_{0.5}MoO_4/MoO_3$, we investigated the degradation activity of the mechanical mixed $Na_{0.5}Ce_{0.5}MoO_4$ and MoO_3 with the same weight ratio as 10% $Na_{0.5}Ce_{0.5}MoO_4/MoO_3$ (denoted as $Na_{0.5}Ce_{0.5}MoO_4$ + MoO_3) (Fig. 10b). Compared with 10% $Na_{0.5}Ce_{0.5}MoO_4/MoO_3$, the photocatalyst of mechanical mixed sample has poor photocatalytic activity. So we think that a strong interaction exists between MoO_3 and $Na_{0.5}Ce_{0.5}MoO_4$, namely, heterojunction has formed, thus remarkably improving the photocatalytic activity of $Na_{0.5}Ce_{0.5}MoO_4/MoO_3$.

The trapping experiments are carried out in the photocatalytic degradation process in order to detect active species. Ammonium oxalate ($(NH_4)_2C_2O_4$) and dimethyl sulfoxide (DMSO) are chosen as the holes and the radical scavengers, respectively. The results are presented in Fig. 11. For pure MoO_3, DMSO has a small effect on its photocatalytic efficiency, while the photodegradation of RhB is inhibited obviously by the addition of ammonium oxalate (Fig. 11a). This result demonstrates that holes (h^+) are the main active species for MoO_3. Nevertheless, for 10% $Na_{0.5}Ce_{0.5}MoO_4/MoO_3$, holes ($h^+$) and hydroxyl radicals ($^{\bullet}OH$) are both the main active species in the degradation of RhB. Moreover, the degradation activity upon adding ammonium oxalate is higher than that upon adding DMSO, suggesting that holes (h^+) plays a more important role than hydroxyl radical ($^{\bullet}OH$) in the degradation process of RhB (Fig. 11b).

In order to understand the degradation process, the degradation of RhB over 10% $Na_{0.5}Ce_{0.5}MoO_4/MoO_3$ was analyzed by total organic carbon (TOC). The TOC result is shown in Fig. S6 (ESI†). It can be observed that after 90 min, the TOC decreases by about 40%, but it does not reach a complete conversion to CO_2 + H_2O. Two possible reasons can be considered. One may be that more time is needed to complete the mineralization under visible light irradiation ($\lambda \geq 420$ nm); the other may be that the dye has been decomposed into small molecules. Limited by our experimental conditions, we can only make a preliminary inference. In fact, this needs further study in the future.

3.5 Activity enhancement mechanism of $Na_{0.5}Ce_{0.5}MoO_4/MoO_3$

On base of the results above, the charge transfer and photocatalytic mechanism over xNa$_{0.5}$Ce$_{0.5}$MoO$_4$/MoO$_3$ heterojunctions is proposed. The transfer and separation efficiency of interfacial charges can be effectively improved by the $Na_{0.5}Ce_{0.5}MoO_4/MoO_3$ heterojunction due to their matched conduction band (CB) and valence band (VB). As illustrated in Fig. 12, the CB (−0.02 eV) of $Na_{0.5}Ce_{0.5}MoO_4$ lies above the CB (0.44 eV) of MoO_3, while the VB (3.36 eV) of MoO_3 lies below that (2.56 eV) of $Na_{0.5}Ce_{0.5}MoO_4$. Thus, a stable heterojunction is easy to form between MoO_3 and $Na_{0.5}Ce_{0.5}MoO_4$. Consequently, an interface electric field forms in the $Na_{0.5}Ce_{0.5}MoO_4/MoO_3$ heterojunction. MoO_3 has a band gap of 2.92 eV, thus it can absorb a part of visible light. Moreover, $Na_{0.5}Ce_{0.5}MoO_4$ has an excellent visible light absorption, thus greatly improving visible light absorption ability of $Na_{0.5}Ce_{0.5}MoO_4/MoO_3$. Under visible

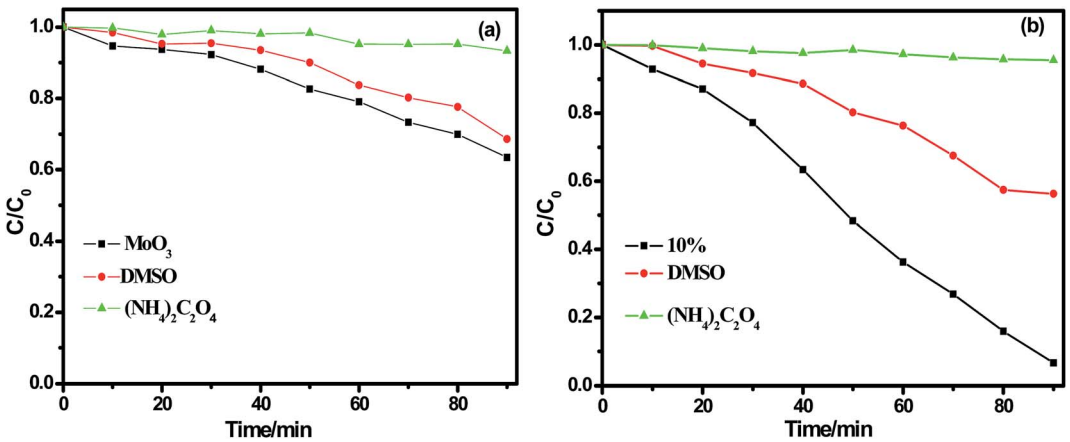

Fig. 11 Trapping experiments for the photodegradation of RhB over (a) MoO_3; (b) 10% $Na_{0.5}Ce_{0.5}MoO_4/MoO_3$ under visible light irradiation ($\lambda \geq$ 420 nm).

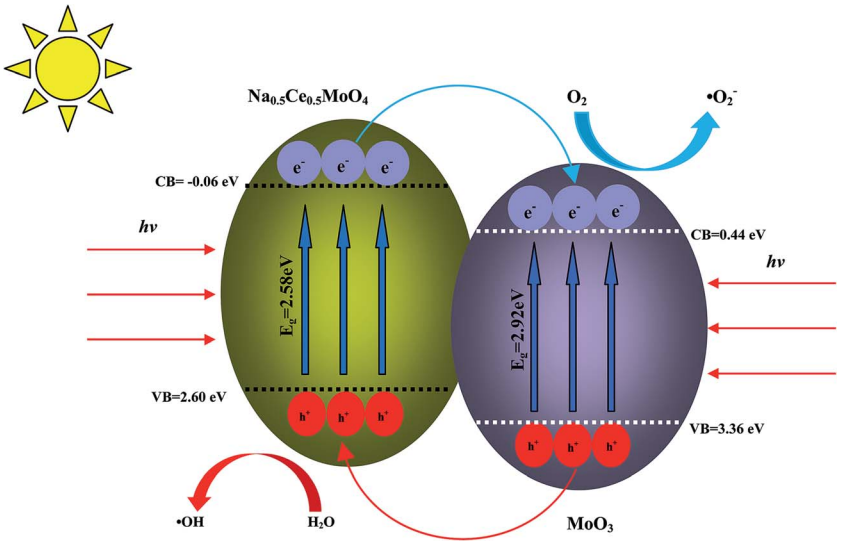

Fig. 12 Proposed photocatalytic degradation and charge transfer mechanism over xNa$_{0.5}$Ce$_{0.5}$MoO$_4$/MoO$_3$ heterojunctions.

light irradiation ($\lambda \geq 420$ nm), both MoO_3 and $Na_{0.5}Ce_{0.5}MoO_4$ can absorb the photons to generate electron–hole pairs. Since the CB of $Na_{0.5}Ce_{0.5}MoO_4$ is more negative than that of MoO_3, the photo-generated electrons at the CB of $Na_{0.5}Ce_{0.5}MoO_4$ can migrate to the CB of MoO_3. Then the electrons stored in the CB of MoO_3 could be trapped by the O_2 near the surface of MoO_3 to form reactive $^{\bullet}O_2^{-}$. Meanwhile, the holes generated in the VB of MoO_3 can move to VB of $Na_{0.5}Ce_{0.5}MoO_4$. Because holes (h^+) and hydroxyl radicals ($^{\bullet}OH$) are both main active species in the photocatalytic process, and holes (h^+) plays a more important role than hydroxyl radical ($^{\bullet}OH$) in the degradation of RhB. The most holes in VB in $Na_{0.5}Ce_{0.5}MoO_4$ can also directly oxidize the organic compounds or react with H_2O to form $^{\bullet}OH$ radicals. Besides, $Na_{0.5}Ce_{0.5}MoO_4$ has a high electrical conductivity, thus, the photogenerated carriers could be easily transferred in xNa$_{0.5}$Ce$_{0.5}$MoO$_4$/MoO$_3$ heterojunctions under the visible light irradiation. As a result, the recombination possibility of electron–hole pairs may be greatly reduced by the interface electric field of $Na_{0.5}Ce_{0.5}MoO_4/MoO_3$ heterojunction, thus improving the photocatalytic activity.[48] As a result, the xNa$_{0.5}$Ce$_{0.5}$MoO$_4$/MoO$_3$ heterojunctions exhibit better photocatalytic properties than that of MoO_3 and $Na_{0.5}Ce_{0.5}MoO_4$ in the degradation of RhB under visible light irradiation ($\lambda \geq 420$ nm).

4. Conclusions

As a new, efficient visible light absorption material, $Na_{0.5}Ce_{0.5}$-MoO_4, has remarkably improved the photocatalytic activity of $Na_{0.5}Ce_{0.5}MoO_4/MoO_3$ heterojunctions under visible light irradiation ($\lambda \geq 420$ nm), which can be employed to prepare the other excellent visible light responsive photocatalysts.

Acknowledgements

This work is financially supported by National Science Foundation of China (21377060), Scientific Research Foundation for the Returned Overseas Chinese Scholars of State Education Ministry (20121707), Six Talent Climax Foundation of Jiangsu (20100292), the Key Project of Environmental Protection Program of Jiangsu (2013005), Natural Science Foundation of Jiangsu province (BK2012464), the Project Funded by the Science and Technology Infrastructure Program of Jiangsu (BM201380277), and A Project Funded by the Priority Academic Program Development of Jiangsu Higher Education Institutions (PAPD) sponsored by SRF for ROCS, SEM (2013S002).

References

1 M. N. Chong, B. Jin, C. W. K. Chow and C. Saint, *Water Res.*, 2010, **44**, 2997–3027.
2 H. L. Zhou, Y. Q. Qu, T. Zeid and X. F. Duan, *Energy Environ. Sci.*, 2012, **5**, 6732–6743.
3 S. Y. Chai, Y. J. Kim, M. H. Jung, A. K. Chakraborty, D. Jung and W. I. Lee, *J. Catal.*, 2009, **262**, 144–149.
4 L. Zhang, K. H. Wong, Z. Chen, J. C. Yu, J. Zhao, C. Hu, C. Y. Chan and P. K. Wong, *Appl. Catal., A*, 2009, **363**, 221–229.
5 N. Q. Wu, J. Wang, D. N. Tafen, H. Wang, J. G. Zheng, J. P. Lewis, X. G. Liu, S. S. Leonard and A. Manivannan, *J. Am. Chem. Soc.*, 2010, **132**, 6679–6685.
6 W. J. Zhou, G. J. Du, P. G. Hu, G. Li, D. Z. Wang, H. Liu, J. Y. Wang, R. I. Boughton, D. Liu and H. D. Jiang, *J. Mater. Chem.*, 2011, **21**, 7937–7945.
7 Q. Z. Wang, J. Hui, L. Yang, H. H. Huang, Y. X. Cai, S. Q. Yin and Y. M. Ding, *Appl. Surf. Sci.*, 2014, **289**, 224–229.
8 K. Kumar, M. Chitkara, I. S. Sandhu, D. Mehta and S. Kumar, *J. Alloys Compd.*, 2014, **588**, 681–689.
9 K. H. Reddy, S. Martha and K. M. Parida, *Inorg. Chem.*, 2013, **52**, 6390–6401.
10 M. S. Palmer, M. Neurock and M. M. Olken, *J. Am. Chem. Soc.*, 2002, **124**, 8452–8846.

11 A. A. Kaminskii, H. J. Eichler, K. I. Ueda, N. V. Klassen, B. S. Redkin, L. E. Li, J. Findeisen, D. Jaque, J. García-Sole, J. Fernández and R. Balda, *Appl. Opt.*, 1999, **38**, 4533–4547.
12 F. Esteban-Betegón, C. Zaldo and C. Cascales, *Chem. Mater.*, 2010, **22**, 2315–2324.
13 L. Xu, X. Y. Yang, Z. Zhai, D. X. Gu, H. Pang and W. H. Hou, *CrystEngComm*, 2012, **14**, 7330–7337.
14 E. Comini, L. Yubao, Y. Brando and G. Sberveglieri, *Chem. Phys. Lett.*, 2005, **407**, 368–371.
15 T. He and J. N. Yao, *J. Photochem. Photobiol., A*, 2003, **4**, 125–143.
16 Z. Hussain, *J. Mater. Res.*, 2001, **16**, 2695–2708.
17 Y. P. Chen, C. L. Lu, L. Xu, Y. Ma, W. H. Hou and J. Zhu, *CrystEngComm*, 2010, **12**, 3740–3747.
18 H. Sinaim, A. Phuruangrat, S. Thongtem and T. Thongtem, *Mater. Chem. Phys.*, 2012, **132**, 358–363.
19 P. Agarwal, I. Paramasivam, N. K. Shrestha and P. Schmuki, *Chem.–Asian J.*, 2010, **5**, 66.
20 A. Chithambararaj, N. S. Sanjini, A. C. Bose and S. Velmathi, *Catal. Sci. Technol.*, 2013, **3**, 1405–1414.
21 T. X. Liu, B. X. Li, Y. G. Hao and Z. Y. Yao, *Chem. Eng. J.*, 2014, **244**, 382–390.
22 Y. P. Li, L. Y. Huang, J. B. Xu, H. Xu, Y. G. Xu, J. X. Xia and H. M. Li, *Mater. Res. Bull.*, 2015, **70**, 500–505.
23 H. Natori, K. Kobayashi and M. Takahashi, *J. Oleo Sci.*, 2009, **58**, 203–211.
24 W. J. Dong, Z. Shi, J. J. Ma, C. M. Hou, Q. Wan, S. H. Feng, A. Cogbill and Z. R. Tian, *J. Phys. Chem. B*, 2006, **110**, 5845–5848.
25 I. Ghaffar, M. F. Warsi, M. Shahid and I. Shakir, *Phys. E*, 2016, **79**, 1–7.
26 L. Y. Huang, H. Xu, R. X. Zhang, X. N. Cheng, J. X. Xia, Y. G. Xu and H. M. Li, *Appl. Surf. Sci.*, 2013, **283**, 25–32.
27 L. Cheng, M. Shao, X. Wang and H. Hu, *Chem.–Eur. J.*, 2009, **15**, 2310–2316.
28 V. M. Mohan, H. Bin and W. Chen, *J. Solid State Electrochem.*, 2010, **14**, 1769–1775.
29 H. C. Zeng, *Inorg. Chem.*, 1998, **37**, 1967–1973.
30 D. Yue, D. M. Chen, Z. H. Wang, H. Ding, R. L. Zong and Y. F. Zhu, *Phys. Chem. Chem. Phys.*, 2014, **16**, 26314–26321.
31 J. Zeng, H. Wang, Y. C. Zhang, M. K. Zhu and H. Yan, *J. Phys. Chem. C*, 2007, **111**, 11879–11887.
32 N. Sahai, *Environ. Sci. Technol.*, 2002, **36**, 445–452.
33 X. Zhang, L. Z. Zhang, T. F. Xie and D. J. Wang, *J. Phys. Chem. C*, 2009, **113**, 7371–7378.
34 S. H. Elder, F. M. Cot, Y. Su, S. M. Heald, A. M. Tyryshkin, M. K. Bowman, Y. Gao, A. G. Joly, M. L. Balmer, C. K. Kolwaite, K. A. Magrini and D. M. Blake, *J. Am. Chem. Soc.*, 2000, **122**, 5138–5146.
35 Y. Ren, M. Chen, Y. Zhang and L. M. Wu, *Langmuir*, 2010, **26**, 11391–11396.
36 M. X. Lu, C. L. Shao, K. X. Wang, N. Lu, X. Zhang, P. Zhang, M. Y. Zhang, X. H. Li and Y. C. Liu, *ACS Appl. Mater. Interfaces*, 2014, **6**, 9004–9012.
37 M. Adachi, M. Sakamoto, J. T. Jiu, Y. Ogata and S. Isoda, *J. Phys. Chem. B*, 2006, **110**, 13872–13880.
38 Y. D. Hou, A. B. Laursen, J. S. Zhang, G. G. Zhang, Y. S. Zhu, X. C. Wang, S. Dahl and I. Chorkendorff, *Angew. Chem., Int. Ed.*, 2013, **52**, 3621–3625.
39 Y. H. Lv, Y. F. Liu, Y. Y. Zhu and Y. F. Zhu, *J. Mater. Chem. A*, 2014, **2**, 1174–1182.
40 C. S. Pan, J. Xu, Y. J. Wang, D. Li and Y. F. Zhu, *Adv. Funct. Mater.*, 2012, **22**, 1518–1524.
41 S. F. Chen, W. Zhao, W. Liu and S. J. Zhang, *Appl. Surf. Sci.*, 2008, **255**, 2478–2484.
42 Y. Liu, Y. X. Yu and W. D. Zhang, *J. Phys. Chem. C*, 2013, **117**, 12949–12957.
43 Y. Y. Zhu, Q. Ling, Y. F. Liu, H. Wang and Y. F. Zhu, *Phys. Chem. Chem. Phys.*, 2015, **17**, 933–940.
44 Y. J. Li, X. D. Li, J. W. Li and J. Yin, *Water Res.*, 2006, **40**, 1119–1126.
45 C. H. Wu, H. W. Chang and J. M. Chern, *J. Hazard. Mater.*, 2006, **137**, 336–343.
46 Y. J. Jin, N. Li, H. Q. Liu, X. Hua, Q. Y. Zhang, M. D. Chen and F. Teng, *Dalton Trans.*, 2014, **43**, 12860–12870.
47 S. R. Dhage, M. S. Hassan and O. B. Yang, *Mater. Chem. Phys.*, 2009, **114**, 511–514.
48 L. W. Zhang, H. B. Fu and Y. F. Zhu, *Adv. Funct. Mater.*, 2008, **18**, 2180–2189.